Spatially entangled photon-pair generation using a partial spatially coherent pump beam

Hugo Defienne* and Sylvain Gigan
Laboratoire Kastler Brossel, ENS-Université PSL, CNRS, Sorbonne Universite, College de France, 24 Rue Lhomond, F-75005 Paris, France

(Received 5 December 2018; published 21 May 2019)

We demonstrate experimental generation of spatially entangled photon pairs by spontaneous parametric down-conversion (SPDC) using a partial spatially coherent pump beam. By varying the spatial coherence of the pump, we show its influence on the down-converted photon's spatial correlations and on its degree of entanglement, in excellent agreement with theory. We then exploit this property to produce pairs of photons with a specific degree of entanglement by tailoring of the pump coherence length. This work thus unravels the fundamental transfer of coherence occurring in SPDC processes, and provides a simple experimental scheme to generate photon pairs with a well-defined degree of spatial entanglement, which may be useful for quantum communication and information processing.

DOI: 10.1103/PhysRevA.99.053831

Quantum entanglement is considered as one of the most powerful resources for quantum information. In this respect, pairs of photons are the simplest system showing genuine quantum entanglement in all their degrees of freedom: spatial, spectral, and polarization [1–3]. Most of the fundamental experiments and related applications are implemented using polarization-entangled photons. Examples range from the first test of Bell's inequality [4] to the recent development of long-distance quantum communication systems [5]. In the last years, there has been renewed interest in continuous variable entanglement between transverse position and momentum of photon pairs [6]. Indeed, their infinite-dimensional Hilbert space holds high potential for developing powerful information processing algorithms [7] and secured cryptography protocols [8]. Furthermore, spatially entangled photon-pair sources are at the basis of many quantum imaging approaches, including ghost imaging [9], sub-shot-noise [10] and sub-Rayleigh imaging [11]. All these quantum applications crucially rely on properties of the down-converted photons. In this respect, their degree of entanglement is a fundamental parameter that generally defines the power of the quantum-based technique. As concrete examples, it sets the information bound in high-dimensional quantum communication systems [12] and the spatial resolution in certain quantum imaging schemes [13]. However, most apparatus used to produce entangled pairs are not flexible and adapting pair characteristics to specific use is generally a challenging task. In this work, we propose an experimental approach based on spontaneous parametric down-conversion (SPDC) with a partial spatially coherent pump beam to produce entangled photon pairs with tunable degree of spatial entanglement.

SPDC is the most popular technique to produce spatially entangled photon pairs. In its conventional form, a coherent Gaussian beam of light (i.e., the pump beam) illuminates a nonlinear crystal (χ^2 nonlinearity) that produces pairs of photons in accordance with energy and momentum conservation [14]. Alternatively, SPDC was also demonstrated using light emitting diodes (LED) [15,16] and continuous-wavelength multimode diode laser [17,18] excitations. Properties of down-converted photons, including their degree of entanglement, are set by the crystal parameters and the pump beam properties [19–23]. During this process, coherence properties of the pump beam get entirely transferred to those of the two-photon field [24–26]. Interestingly, none of these experimental studies consider the use of a nonperfectly spatially coherent pump beam to produce photon pairs, with the notable exception of the recent work of Ismail *et al.* [26] that investigates polarization entanglement between photons. Theoretically, the link between spatial coherence properties of the pump and the degree of entanglement of the down-converted field has been precisely established in [27,28]. In this work, we first investigate experimentally the influence of the pump spatial coherence on the correlation properties of the spatially entangled photon pairs. We then demonstrate the dependency of the degree of entanglement, characterized by the Schmidt number [29–31], with the coherence of the pump. Finally, we exploit this effect to generate photon pairs with a well-defined degree of entanglement by manipulating the transverse coherence length of the pump.

Figure 1(a) shows the apparatus used to produce spatially entangled photon pairs. A partially coherent beam of light is generated by intercepting the propagation path of a continuous-wavelength (405 nm) Gaussian laser beam with a (rotating or not) random diffuser (plastic sleeve). Blue photons interact with a tilted nonlinear crystal of β-barium borate (BBO) to produce infrared pairs of photons by type-I SPDC. At the output of the crystal, transverse momentum $\mathbf{k}$ of photons is mapped onto pixels of an electron multiplied charge coupled device (EMCCD) camera by a Fourier-lens imaging system (f_3). The camera allows direct intensity measurements, providing conventional intensity images (black-red colorscale), and correlation intensity measurements (blue-red colorscale), giving the joint probability distribution Γ of photon pairs. The technique used to measure Γ is described

*hugo.defienne@gmail.com

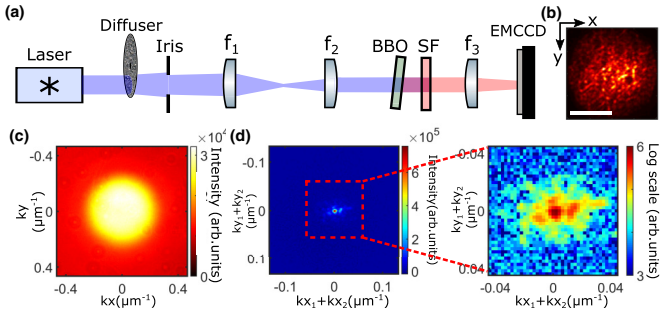

FIG. 1. (a) Light emitted by a diode laser ($\lambda_p = 405$ nm) is scattered by a static thin diffuser (plastic sleeve) and illuminates a nonlinear crystal of β-barium borate (BBO) to produce spatially entangled pairs of photons by type-I SPDC. Spectral filters at 810 ± 10 nm select near-degenerate photons. Lenses $f_1 = 150$ mm and $f_2 = 200$ mm image an iris onto the crystal surface. When the diffuser is maintained fixed, the crystal is thus illuminated by a static speckle pattern (b). White scale bar corresponds to 700 μm. Momenta of photons are imaged onto an EMCCD camera by imaging the far field via a $f_3 = 40$-mm lens, and a direct intensity image (c) is recorded by accumulating photons onto an EMCCD camera sensor. Sum-coordinate projection of the joint probability distribution of photon pairs (d) shows a coincidence speckle pattern that reveals the transfer of coherence between the pump and the down-converted fields. Black-red and blue-red colorbars correspond, respectively, to intensity and intensity correlation measurements.

in [32] and relies on two main assumptions that are verified in this experiment: The power of the continuous-wavelength pump laser is sufficiently low to neglect higher-order generation processes ($\sim$100 mW) and cross-talks between pixels of the camera are negligible (see Appendix E). Note that this detection technique directly removes the correlation background due to accidental photon coincidences (i.e., coincidences between photons from different pairs). Throughout this work, Γ is visualized using two types of bidimensional projections: sum-coordinate and X_+-coordinate projections. A sum-coordinate projection represents the probability of detecting the two photons with symmetric momentum relative to their mean $\mathbf{k_1} + \mathbf{k_2}$ and a X_+-coordinate projection represents the joint probability of detecting one photon with momentum k_{y_1} (k_{x_1} can take any possible values) and its twin with momentum k_{y_2} and $k_{x_2} = -k_{x_1}$ [33–35] (see Appendix F for more details on the detection technique and the Γ projections).

When the diffuser is maintained static, the crystal is illuminated by a speckle pattern [Fig. 1(b)]. A direct intensity image [Fig. 1(c)] is acquired by photon accumulation on the camera sensor and shows a homogeneous structure, very similar to the one observed without diffuser [Fig. 2(a1)]. However, when measuring the joint probability distribution Γ with the EMCCD camera, its projection along the sum-coordinate diagonal shows a central peak surrounded by a speckle pattern [Fig. 1(c)]. The presence of this speckle together with the absence of any spatial structure in the direct intensity image demonstrates that first-order spatial coherence of the pump field (i.e., intensity speckle pattern) gets entirely transferred to second-order coherence of the down-converted field (i.e., coincidence speckle pattern).

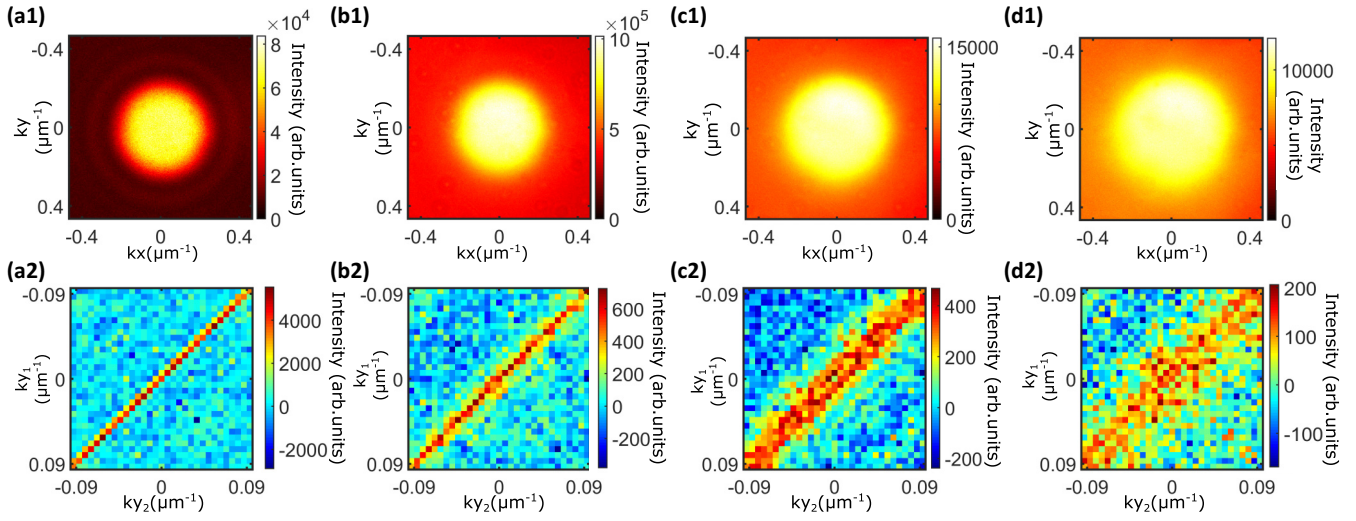

FIG. 2. Without diffuser, the direct intensity image (a1) shows a well-defined disk and the X_+-coordinate projection of Γ (a2) shows a strong antidiagonal. An element (ky_1, ky_2) of the X_+-coordinate projection corresponds to the joint probability of detecting one photon at $\mathbf{k_1} = (k_{x_1}, k_{y_1})$, with no constraints on k_{x_1}, together with the second photon at $\mathbf{k_2} = (-k_{x_1}, k_{y_2})$. The strong antidiagonal is a signature of momentum conservation between photons produced by SPDC with a fully coherent collimated pump beam. When a rotating random diffuser composed by one layer of plastic sleeve is introduced in the apparatus, edges of the direct intensity disk gets blurred (b1) and the width of the antidiagonal on the X_+-coordinate projection increases (b2). When one photon is detected at $\mathbf{k}$, its twin has now a high probability to arrive on an area that spreads around $-\mathbf{k}$. This area broadens when the coherence length of the pump is decreased by using rougher random diffusers, as shown on direct images (c1) and (d1) and X_+-coordinate projections (c2) and (d2) measured using, respectively, two layers of plastic sleeve and three layers. Correlation measurements are performed by acquiring a total number of images between 4×10^5 (no diffuser) and 2×10^7 (three layers) with an exposure time set between 5 and 30 ms. Black-red and blue-red colorbars correspond, respectively, to intensity and intensity correlation measurements.

As a consequence, spatial incoherence properties of the pump must be retrieved in the momentum correlations of the pairs. When the diffuser is rotated faster than the camera integration time, the pump acts as a partial spatially coherent beam. Using a Gaussian-Schell model for the pump beam [36] and a Gaussian approximation for the down converted field [37,38] (see Appendix A) Γ is written as

$$\Gamma(\mathbf{k_1},\mathbf{k_2}) \sim \exp\left(-\frac{\sigma_r^2|\mathbf{k_1}-\mathbf{k_2}|^2}{2}\right)\exp\left(-\frac{|\mathbf{k_1}+\mathbf{k_2}|^2}{2\sigma_k^2}\right). \tag{1}$$

The position-correlation width σ_r only depends on the crystal length L and the pump frequency λ_p as $\sigma_r = \sqrt{\alpha L\lambda_p/(2\pi)}$ ($\alpha = 0.455$ [39]). The momentum-correlation width σ_k depends on the pump beam waist ω and its correlation length ℓ_c as

$$\sigma_k = \sqrt{\frac{1}{\ell_c^2}+\frac{1}{4\omega^2}}. \tag{2}$$

For a given crystal, varying the coherence properties of the pump beam (i.e., waist and correlation length) modifies the spatial structure of the two-photon wave function and its associated joint probability distribution. In particular, decreasing the correlation length at fixed waist induces an increase of the momentum-correlation width: When one photon of a pair is detected at $\mathbf{k}$, the area of maximum probability detection for its twin is centered at $-\mathbf{k}$ and spreads as $\sigma_k^2 \sim \ell_c^{-2}$. This effect is shown in Fig. 2. For a perfectly coherent pump beam (no diffuser), the direct intensity image [Fig. 2(a1)] shows a well-defined homogeneous disk and the X_+-coordinate projection of Γ [Fig. 2(a2)] shows a strong antidiagonal. Such a strong antidiagonal is a clear signature of transverse momentum conservation in SPDC using a collimated pump beam. When a rotating diffuser is used (single layer of plastic sleeve), the pump beam becomes partially coherent which results in a blurring of the edges of the direct intensity disk [Fig. 2(b1)] and an increase of the diagonal width in the X_+-coordinate projection [Fig. 2(b2)]. Broadening of momentum correlations with the decrease of pump spatial coherence shows very well when using rougher diffusers, respectively, made by superimposing two layers of plastic sleeves [Figs. 2(c1) and 2(c2)] and three layers [Figs. 2(d1) and 2(d2)]. A quantitative analysis of this effect is provided in Fig. 3. On the one hand, values of σ_k are determined by fitting sum-coordinate projection of Γ (see Appendix B) by a Gaussian model [37,38]. On the other hand, values of ℓ_c are measured by removing the crystal and Fourier imaging the pump beam directly onto the camera (see Appendix D). The linear regression of $\sigma_k^2 = f(1/\ell_c^2)$ [Fig. 3(a)] returns a slope value of 0.8 ± 0.3. This result is in good accordance with Eq. (2) and its underlying theoretical model [27,28] (fitting details in Appendix E).

Not only does partial coherence influence momentum correlations between pairs, but it also modifies their degree of entanglement, that can be quantified by the Schmidt number. For a mixed state, it is defined as the minimum Schmidt number of the pure states composing it [30,31]. In this work, it is estimated from the Schmidt number K of a virtual pure two-photon state generated by a pump beam of diameter σ_k^{-1} using the formula $K = 1/4[1/(\sigma_r\sigma_k) + \sigma_r\sigma_k]^2$ [29]. Indeed,

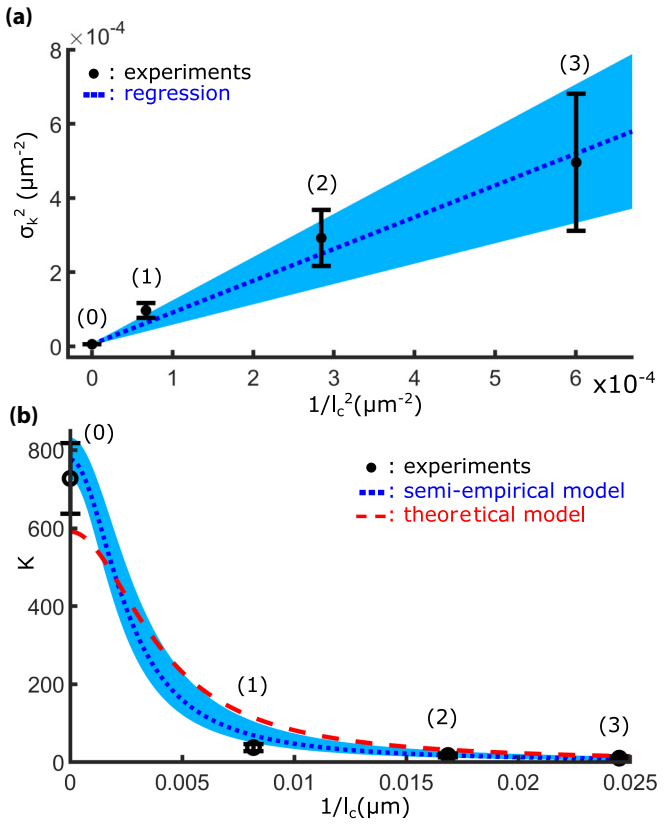

FIG. 3. (a) Momentum-correlation width σ_k is represented in the function of coherence length of the pump ℓ_c. Values on the graph correspond to four different measurements performed (0) without diffuser, (1) with one layer of plastic sleeve, (2) two layers, and (3) three layers. Linear regression fits experimental values and returns a slope of 0.8 ± 0.3 (blue dashed line and shaded area), in accordance with Eq. (2). (b) Schmidt number K is represented in the function of the coherence length of the pump $1/\ell_c$ (black circles). The blue dashed curve and the shaded area are a semiempirical model obtained by combining results of the linear regression of σ_k with the theoretical formula of σ_r and the K formula [29]. The red dashed curve is a pure theoretical prediction obtained by inserting known experimental parameters (crystal and pump properties) into Eq. (3).

the partially coherent pump beam can be modeled as a mixture of many small coherent beams of diameter σ_K^{-1} that each produce a two-photon pure state. The mixed state can then be written as an incoherent superposition of these pure states and its Schmidt number inferred from their minimum Schmidt number value. Experimentally, while σ_k is determined using the apparatus described previously (Fig. 1), values of σ_r are measured using a different experimental configuration in which the output surface of the crystal is imaged onto the EMCCD camera (see Appendix C). Figure 3(b) shows that K decreases with the reduction of the correlation length ℓ_c (black points). Experimental data shows a good agreement with a semiempirical model (blue dashed line). It is computed from the K formula [29] by using the results of the linear regression in Fig. 3(a) ($\sigma_k^2 \sim 1/\ell_c^2$) together with the theoretical formula of σ_r (see Appendix E).

Values of K can also be estimated only from known experimental parameters (crystal and pump laser properties) using

the theoretical model [Eq. (1)],

$$K_{th} = \frac{1}{4}\left[\frac{2\omega l_c\sqrt{2\pi}}{\sqrt{\alpha L\lambda_p\left(l_c^2+4\omega^2\right)}} + \frac{\sqrt{\alpha L\lambda_p\left(l_c^2+4\omega^2\right)}}{2\omega l_c\sqrt{2\pi}}\right]^2, \quad (3)$$

with $L \approx 0.9$ mm (crystal thickness), $\lambda_p \approx 405$ nm (pump wavelength), $\alpha = 0.455$ [39], and $\omega \approx 125$ μm (pump waist). K_{th} is shown in Fig. 3(b) as a red dashed line. We observe an order of magnitude agreement between theoretically expected values of K and those measured experimentally. Knowing the characteristics of the crystal and the pump therefore allows predicting reasonably well the degree of entanglement of the source. For a given crystal, we show that manipulating the pump coherence using rotating random diffusers enable the deterministic control of the degree of entanglement in the two-photon field generated.

The future of quantum optical technologies depends on our capacity to detect [32,40,41] and manipulate photons [42,43], but it also crucially relies on our ability to generate photons with properties adapted to specific application. In our work, we show how to produce spatially entangled photons with a specific degree of entanglement by controlling the spatial coherence of the pump beam with rotating random diffusers. For this, we investigated the fundamental transfer of coherence between the pump and the down-converted field and showed a good agreement with the theory [27,28]. This novel source may play an important role in free-space quantum communications, since it has been recently shown in theory that a two-photon field is less susceptible to atmospheric turbulence when it was generated by a partial spatially coherent beam [44]. In this respect, the use of a spatial light modulator in place of the random diffusers will be the next natural step to enable tailoring entanglement in real time and use it as a tunable parameter to produce quantum states that are optimal for a given protocol and strength of turbulence. Incoherent two-photon illumination could also play an important role in optical imaging to improve resolution [45]. Finally, this work may have technological impact as it paves the way towards the development of cheap and compact photon-pair sources using light emitting diodes as pump beams [46].

Note added in proof. Recently, a new work on spatially entangled photon-pair generation by a spatially incoherent pump was reported by Zhang *et al.* [47].

Acknowledgments

This work was funded by the European Research Council (ERC) (724473); S.G. is a member of the institut universitaire de France (IUF).

APPENDIX A: THEORETICAL MODEL

1. Joint probability distribution in momentum-space $\Gamma(\mathbf{k_1}, \mathbf{k_2})$

As demonstrated in [28] [Eq. (B8)], the joint probability distribution $\Gamma(\mathbf{k_1}, \mathbf{k_2})$ for a partial spatially coherent pump beam is written as

$$\Gamma(\mathbf{k_1}, \mathbf{k_2}) \sim |\tilde{\chi}(|\mathbf{k_1}-\mathbf{k_2}|^2)|^2 \tilde{V}(\mathbf{k_1}+\mathbf{k_2}, \mathbf{k_1}+\mathbf{k_2}), \quad (A1)$$

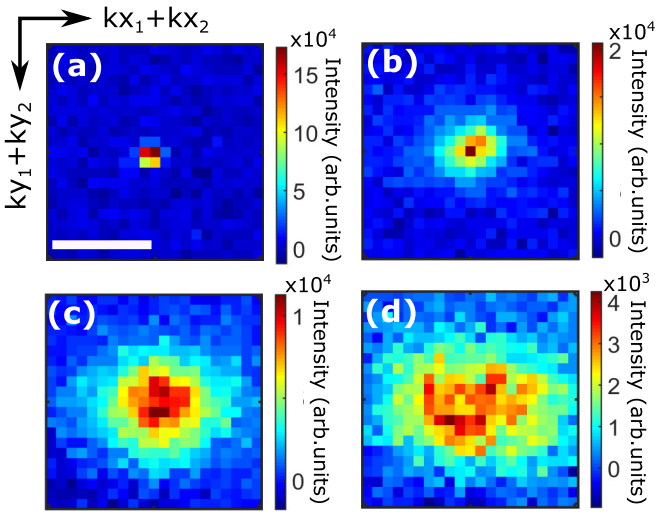

FIG. 4. Sum-coordinate projections of Γ measured with (a) no diffuser, (b) one-layer rotating diffuser, (c) two layers, and (d) three layers. Values of σ_k are estimated in each case by measuring the width of the central spot using a Gaussian model [37,38]. White scale bar corresponds to 0.05 μm^{-1}.

where $\tilde{\chi}$ is the phase-matching function and $\tilde{V}$ is the transverse momentum-correlation function of the pump field. In our work, we use two distinct approximations.

(1) A Gaussian approximation [37,38] for $\tilde{\chi}$:

$$|\tilde{\chi}(|\mathbf{k_1}-\mathbf{k_2}|^2)|^2 \sim \exp\left[-\frac{\sigma_r^2|\mathbf{k_1}-\mathbf{k_2}|^2}{2}\right], \quad (A2)$$

where $\sigma_r = \sqrt{\alpha L\lambda_p/(2\pi)}$, λ_p is the pump wavelength, L the crystal length, and $\alpha = 0.455$ [39].

(2) A Gaussian-Schell approximation [36] for the partial spatially coherent pump beam, which results in $\tilde{V}$ being written as

$$\tilde{V}(\mathbf{k}, \mathbf{k}') \sim \exp\left[-\frac{\omega^2|\mathbf{k}-\mathbf{k}'|^2}{2} - \frac{|\mathbf{k}+\mathbf{k}'|^2}{8\sigma_k^2}\right], \quad (A3)$$

where $\sigma_k = \sqrt{1/l_c^2 + 1/(4\omega^2)}$, with l_c the coherence length of the pump and ω its waist.

Combining Eqs. (A2), (A3), and (A1) leads to Eq. (1).

2. Sum-coordinate projection of $\Gamma(\mathbf{k_1}, \mathbf{k_2})$

The sum-coordinate projection of Γ, denoted P_+^Γ, is calculated by integrating Eq. (1) along $\mathbf{k_1}+\mathbf{k_2}$ and takes the simple form,

$$P_+^\Gamma(\mathbf{k_1}+\mathbf{k_2}) \sim \exp\left(-\frac{|\mathbf{k_1}+\mathbf{k_2}|^2}{2\sigma_k^2}\right). \quad (A4)$$

APPENDIX B: σ_k MEASUREMENTS AND UNCERTAINTIES

Values of σ_k are determined by fitting sum-coordinate projections of Γ with a Gaussian function [Eq. (A4)]. Figure 4 shows images of the sum-coordinate projections measured with (a) no diffuser, (b) one-layer rotating diffuser, (c) two layers, and (d) three layers.

TABLE I. Values of σ_k, σ_k^2, $\Delta\sigma_k$, $\Delta\sigma_k^2$, ΔN. Units are μm^{-1}.

	No diffuser	One layer	Two layers	Three layers
ΔN	2.23×10^{-2}	4.09×10^{-2}	6.65×10^{-2}	8.90×10^{-2}
σ_k	2.4×10^{-3}	9.8×10^{-3}	1.7×10^{-2}	2.2×10^{-2}
σ_k^2	5.6×10^{-6}	9.7×10^{-5}	2.9×10^{-4}	4.97×10^{-4}
$\Delta\sigma_k$	7.8×10^{-5}	1.0×10^{-3}	2.2×10^{-3}	4.2×10^{-3}
$\Delta(\sigma_k^2)$	3.7×10^{-7}	2.0×10^{-5}	7.6×10^{-5}	1.8^{-4}
$\Delta\sigma_k/\sigma_k$	3%	10%	12%	18%
$\Delta(\sigma_k^2)/\sigma_k^2$	6%	20%	24%	36%

The fitting model takes the form,

$$f(x, y) = ae^{-\frac{(x-b)^2+(y-c)^2}{2\sigma_k^2}} + d, \tag{B1}$$

where $\{a, b, c, d, \sigma_k\}$ are fitting parameters. Uncertainties $\Delta\sigma_k$ originate from the presence of noise ΔN in the sum-coordinate images that alter the precision of the fit. The link between ΔN and $\Delta\sigma_k$ is given by the value of $grad[f]$ at the position $(x, y) = (\sigma_k/\sqrt{2}, \sigma_k/\sqrt{2})$, giving the following formula:

$$\Delta\sigma_k = \frac{\sigma_k e^{1/2}}{a}\Delta N. \tag{B2}$$

Values of ΔN are measured from the sum-coordinate images. Then, uncertainties $\Delta(\sigma_k^2)$ are calculated by error propagation: $\Delta(\sigma_k^2) = 2\sigma_k\Delta\sigma_k$. All values are reported in Table I.

APPENDIX C: CORRELATION POSITIONS AND σ_r MEASUREMENTS

1. Position correlations

Position correlations between pairs of photons are observed by imaging the output surface of the crystal and measuring the joint probability distribution Γ, as shown in Fig. 5(a). The diffuser is maintained static and is the same as the one used in Fig. 1. The direct intensity image [Fig. 5(b)] is acquired by photon accumulation on the camera sensor and shows a speckle structure. When measuring the joint probability distribution Γ with the EMCCD camera [32,40], its projection along the minus-coordinate diagonal shows a central peak [Fig. 5(c)]. The minus-coordinate projection image represents the probability of detecting two photons from a pair separated by a (oriented) distance $r_1 - r_2$ [33,34]. The strong peak at the center is a clear signature of the strong correlations in position between pairs of photons.

2. σ_r measurements using partially coherent pump beams

Values of σ_r are determined using the experimental setup described Fig. 5(a). The same rotating diffusers (respectively, composed by one, two, and three layers of plastic sleeve) as those of Figs. 2 and 3 are used to generate partially coherent pump beams with different correlation lengths. Interestingly, Fig. 6 shows that neither the direct intensity images [Figs. 6(a1)–6(d1)] nor the X_--coordinate projections [Figs. 6(a2)–6(d2)] depend on the coherence properties of the pump beam. The X_--coordinate image represents the joint probability of detecting one photon at position y_1 (x_1 can take any possible values) and its twin with momentum y_2 and $x_2 \approx x_1$ (see Sec. F). The strong diagonal is a clear signature of position correlations: Both photons are always produced at the same position in the crystal during the SPDC process, and this property does not depend on the coherence properties of the pump beam.

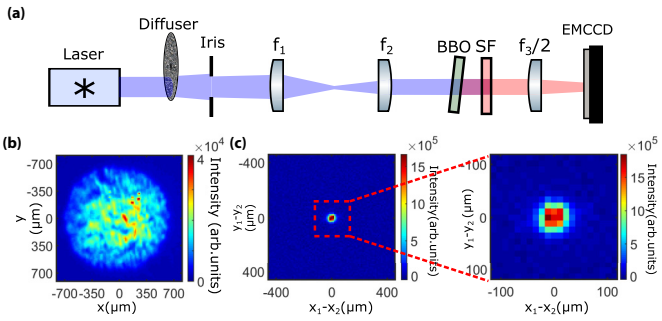

FIG. 5. (a) Light emitted by a diode laser ($\lambda_p = 405$ nm) is scattered by a static thin diffuser (plastic sleeve) and illuminates a nonlinear crystal of β-barium borate (BBO) to produce spatially entangled pairs of photons by type-I SPDC. Spectral filters at 810 ± 10 nm select near-degenerate photons. Lenses $f_1 = 150$ mm and $f_2 = 200$ mm image an iris onto the crystal surface. When the diffuser is maintained fixed, the crystal is thus illuminated by a static speckle pattern. White scale bar corresponds to 700 μm. Positions of photons at the output surface of the crystal are imaged onto an EMCCD camera via a single-lens imaging system $f_3/2 =$ 20 mm. The direct intensity image (b) recorded by accumulating photons onto an EMCCD camera sensor is a speckle pattern. Minus-coordinate projection of the joint probability distribution of photon pairs (c) shows a strong peak at its center that reveals the strong correlations between positions of the pairs.

Similarly to the calculations of section A and those of [28], the use of a Gaussian approximation [37,38] and a Gaussian-Schell model [36] allows writing the joint probability distribution $\Gamma(\mathbf{r_1}, \mathbf{r_2})$ as

$$\Gamma(\mathbf{r_1}, \mathbf{r_2}) \sim \exp\left(-\frac{|\mathbf{r_1} - \mathbf{r_2}|^2}{2\beta\sigma_r^2}\right)\exp(-2\omega^2|\mathbf{r_1} + \mathbf{r_2}|^2), \tag{C1}$$

where ω is the pump beam waist and $\beta = (\alpha + \alpha^{-1})/\alpha$ ($\alpha =$ 0.455 [39]). The minus-coordinate projection of Γ, denoted P_-^Γ, is calculated by integrating Eq. (D3) along $\mathbf{r_1} - \mathbf{r_2}$ and takes the simple form,

$$P_-^\Gamma(\mathbf{r_1} - \mathbf{r_2}) \sim \exp\left(-\frac{|\mathbf{r_1} - \mathbf{r_2}|^2}{2\beta\sigma_r^2}\right). \tag{C2}$$

The minus-coordinate projection images acquired for different correlation lengths are shown in Figs. 6(a3)–6(d3).

3. σ_r measurements and uncertainties

Values of σ_r are determined by fitting minus-coordinates projections of Γ with a Gaussian function [Eq. (C2)]. Figures 6(a3)–6(d3) show images of the minus-coordinate projections measured with (a) no diffuser, (b) one-layer rotating diffuser, (c) two layers, and (d) three layers. The fitting model takes the form,

$$f(x, y) = ae^{-\frac{(x-b)^2+(y-c)^2}{2\sigma_r^2}} + d, \tag{C3}$$

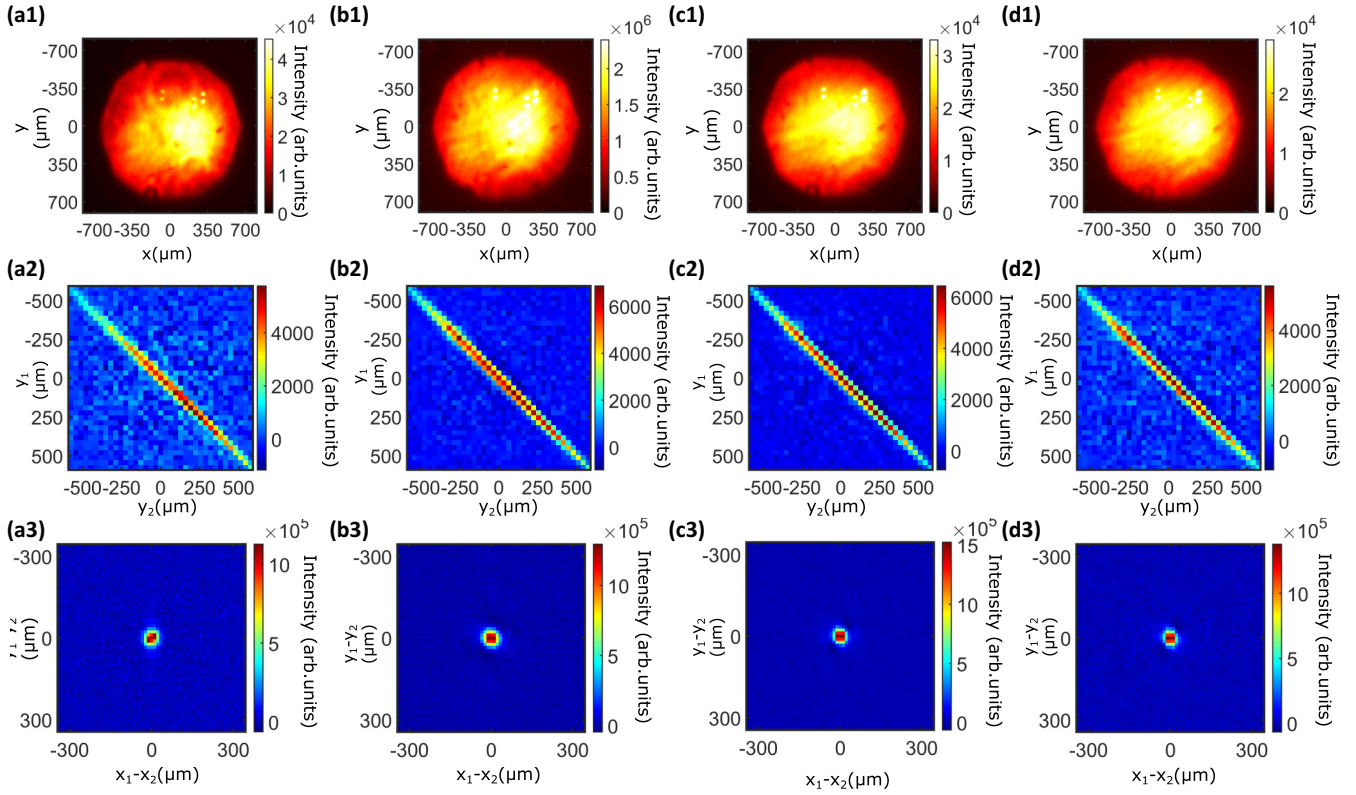

FIG. 6. Direct intensity of the down-converted field at the crystal plane is imaged onto the EMCCD camera using the experimental configuration described in Fig. 5(a) without diffuser (a1), with a rotating diffuser composed by one layer of plastic sleeve (b1), two layers (c1), and three layers (d1). All intensity patterns are homogeneous and identical. When the camera is used to measure the joint probability distribution Γ, the X_--coordinate projection of Γ (see Sec. F) camera shows a very strong diagonal in all four cases: without diffuser (a2), with one layer of plastic sleeve (b2), two layers (c2), and three layers (d2). These projections show that position correlations do not depend on the coherence properties of the pump. Minus-coordinate projections of Γ taken without diffuser (a3), with one layer (b3), two layers (c3), and three layers (d3) show the same peak at their center, which highlights the strong correlations between positions of the pairs. Fitting these images with the model of Eq. (C2) allows determining values of σ_r reported in Table II.

where $\{a, b, c, d\}$ are fitting parameters. Uncertainties $\Delta\sigma_r$ originate from the presence of noise ΔN in the minus-coordinate images that alter the precision of the fit. The link between ΔN and $\Delta\sigma_r$ is given by the value of $grad[f]$ at the position $(x, y) = (\sigma_r/\sqrt{2}, \sigma_r/\sqrt{2})$, giving the following formula:

$$\Delta\sigma_r = \frac{\sigma_r e^{1/2}}{a}\Delta N. \tag{C4}$$

Values of ΔN are measured from the minus-coordinates images. All measured values are reported in Table II.

TABLE II. Values of σ_r, $\Delta\sigma_r$, ΔN. Units are μm.

	No diffuser	One layer	Two layers	Three layers
ΔN	1.86×10^{-2}	1.25×10^{-2}	1.17×10^{-2}	1.57×10^{-2}
σ_r	18.6	20.2	17.2	17.2
$\Delta\sigma_r$	0.6	0.4	0.3	0.4
$\Delta\sigma_r/\sigma_r$	3%	2%	2%	2%

APPENDIX D: PUMP BEAM ANALYSIS AND COHERENCE LENGTH ℓ_c MEASUREMENT

Properties of the pump beam, namely its waist ω and correlation length ℓ_c, are measured using the two experimental configurations described in Figs. 7(a) and 7(b).

1. Intensity distribution of the pump beam in the crystal plane

The intensity distribution of the pump beam in the crystal plane is measured using the experimental configuration described in Fig. 7(b). Figures 7(c)–7(f) show results of four acquisitions performed without diffuser [Fig. 7(c)], with a rotating diffuser composed by one layer of plastic sleeve [Fig. 7(d)], two layers [Fig. 7(e)], and three layers [Fig. 7(f)]. Since the diffusers rotate with a period much shorter than the acquisition time of the camera, the distribution of pump intensity at the crystal plane is homogeneous and does not depend on the coherence properties of the pump.

2. Beam waist and correlation length measurements

Measurements of ω and ℓ_c are performed using the experimental configuration of Fig. 1(a). In this case, the pump field at the crystal plane is Fourier imaged onto the EMCCD

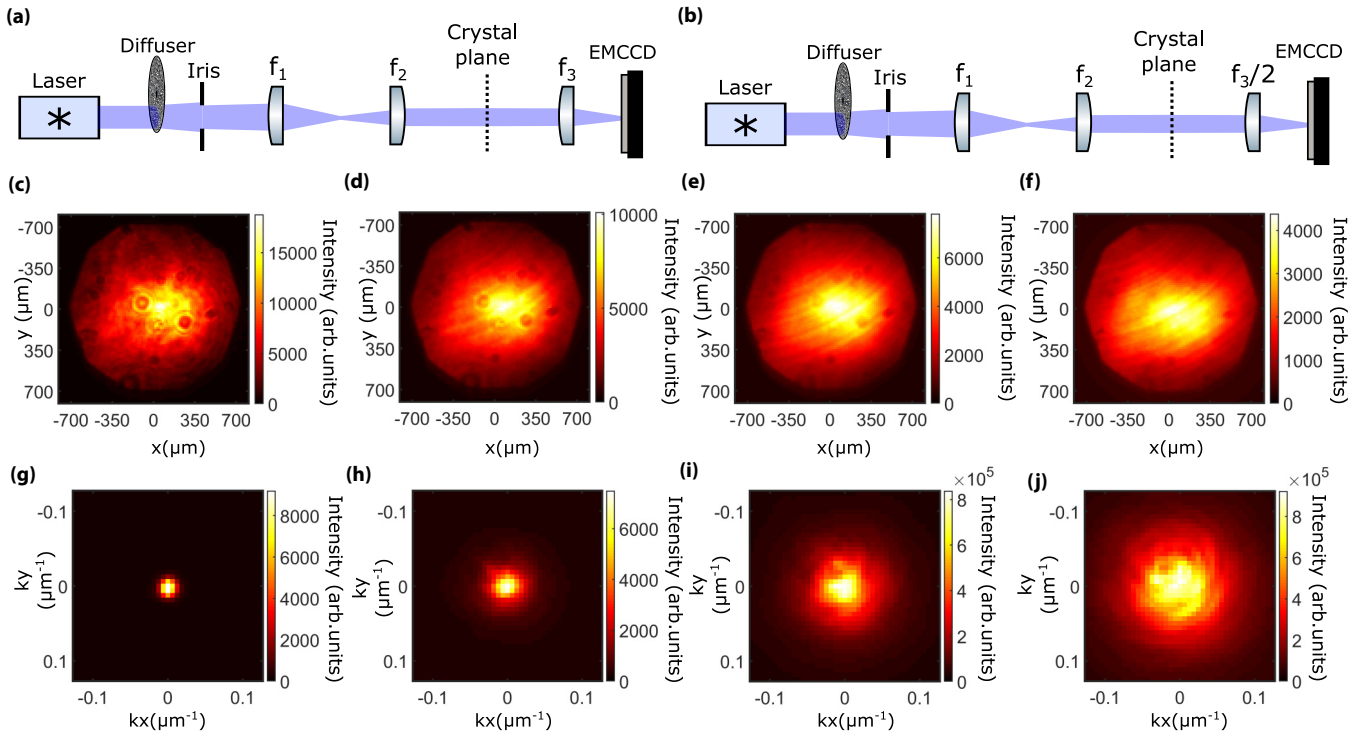

FIG. 7. (a) Apparatus used to Fourier image the pump field at the crystal plane onto the camera. It is similar to the one shown in Fig. 1(a) without the crystal and all the filters. (b) Apparatus used to image the pump field at the crystal plane onto the camera. It is similar to the one shown in Fig. 5(a) without the crystal and all the filters. Using configuration (b), intensity distribution of the pump beam at the crystal plane is imaged on the camera without diffuser (c), with a rotating diffuser composed of one layer of plastic sleeve (d), two layers (e), and three layers (f). All intensity patterns are homogeneous and identical. Using configuration (b), intensity distribution of the pump beam in the momentum space is imaged on the camera without diffuser (g), with a rotating diffuser composed of one layer of plastic sleeve (h), two layers (i), and three layers (j). Without diffuser, the pump beam is focused onto the camera and the width of the peak σ_{p_0} is used to estimate the beam waist $\omega = 1/\sigma_{p_0} \approx 125\ \mu$m. When rotating diffusers are inserted, the peak broadens and its width σ_p provides an estimation of the correlation length ℓ_c using the formula $\ell_c = 2/\sqrt{\sigma_p^2 - \sigma_{p_0}^2}$. Values of ℓ_c are reported in Table III.

camera via lens f_3. Figures 7(g)–7(j) show four direct intensity images acquired, respectively, without diffuser [Fig. 7(g)], with a rotating diffuser composed by one layer of plastic sleeve [Fig. 7(h)], two layers [Fig. 7(i)], and three layers [Fig. 7(j)]. For a perfectly coherent pump, the width of the focus (denoted σ_{p_0}) in Fig. 7(g) is inversely proportional to the beam waist ω,

$$\omega = \frac{1}{\sigma_{p_0}}. \tag{D1}$$

Fitting this intensity distribution by Gaussian model provides an estimation of $\omega \approx 89\ \mu$m. For partially coherent pump beams, intensity distributions in the Fourier domain shown in Figs. 7(h)–7(j) are written as

$$I_p(\mathbf{k_p}) \sim \exp\left[-\frac{|\mathbf{k_p}|^2}{2\sigma_p^2}\right], \tag{D2}$$

where $\sigma_p = 2\sqrt{1/\ell_c^2 + 1/(4\omega^2)}$ (Gaussian-Schell model [36]). Fitting these distributions with Eq. (D2) allows determining σ_p in each case and calculating ℓ_c with the formula,

$$\ell_c = \frac{2}{\sqrt{\sigma_p^2 - \sigma_{p_0}^2}}. \tag{D3}$$

Values of ℓ_c are reported in Table III.

APPENDIX E: DETAILS OF THE FITTING IN FIG. 3

1. Linear fitting in Fig. 3(a)

Experimental data in Fig. 3(a) are fitted with a linear model of the form,

$$f\left(1/\ell_c^2\right) = \frac{a}{\ell_c^2} + \sigma_k^2\left(\ell_c^{-2} = 0\right), \tag{E1}$$

where a is a fitting parameter and $\sigma_k^2(\ell_c^{-2} = 0)$ is the value of σ_k^2 measured at $\ell_c^{-2} = 0$. Uncertainty Δa originates mostly

TABLE III. Values of σ_p in μm^{-1} and ℓ_c in μm.

	No diffuser	One layer	Two layers	Three layers
σ_p	8.0×10^{-3}	1.8×10^{-2}	3.5×10^{-2}	5.0×10^{-2}
ℓ_c	$+\infty$	122	59	41

from the uncertainty of the value of $\sigma_k^2(\ell_c^{-2} = 6 \times 10^{-4})$ measured with three diffusers (36% error). The link between Δa and $\Delta(\sigma_k^2(\ell_c^{-2} = 6 \times 10^{-4}))$ is then given by the following formula:

$$\Delta a = \Delta\big(\sigma_k^2\big(\ell_c^{-2} = 6 \times 10^{-4}\big)\big)\ell_c^2, \tag{E2}$$

which gives $a = 0.8$ and $\Delta a = 0.3$. The blue shaded area in Fig. 3(a) corresponds to values located between the two linear curves: $f_{\max} = \frac{a+\Delta a}{\ell_c^2} + \sigma_k^2(\ell_c^{-2} = 0) + \Delta(\sigma_k^2(\ell_c^{-2} = 0))$ and $f_{\min} = \frac{a-\Delta a}{\ell_c^2} + \sigma_k^2(\ell_c^{-2} = 0) - \Delta(\sigma_k^2(\ell_c^{-2} = 0))$.

2. Theoretical curves in Fig. 3(b)

Figure 3(b) shows values of K measured experimentally (black points) together with a semiempirical model (blue dashed line and blue shaded area) and a theoretical model (red dashed curve). The semiempirical model is computed using the formula $K = 1/4[1/\sigma_k\sigma_r + \sigma_k\sigma_r]^2$ with the following.

(1) The results of the linear regression in Fig. 3(a): $\sigma_k^2 = 0.8/\ell_c^2 + \sigma_k^2(\ell_c^{-2} = 0)$.

(2) A value of σ_r calculated using the theoretical formula: $\sigma_r = \sqrt{L\lambda_p/2\pi} \approx 7.6\ \mu$m.

Borders of the blue shaded area correspond to the two extreme cases for the slope coefficient $0.8 + 0.3 = 1.1$ and $0.8 - 0.3 = 0.5$.

The theoretical model (red dashed curve) is computed from Eq. (3) with $L = 0.9$ mm (crystal thickness), $\lambda_p = 405$ nm (pump wavelength), $\alpha = 0.455$ [39], and $\omega = 125\ \mu$m (pump waist).

APPENDIX F: IMAGE PROCESSING

1. Measurement process

We use an EMCCD Andor Ixon Ultra 897 to measure the joint probability distribution Γ of spatially entangled photon pairs using a technique described in [32]. The camera was operated at $-60°$C, with a horizontal pixel shift readout rate of 17 Mhz, a vertical pixel shift every 0.3 μs, and a vertical clock amplitude voltage of +4V above the factory setting. When the camera is illuminated by photon pairs, a large set of images is first collected using an exposure time chosen to have an intensity per pixel approximately 5 times larger than the mean value of the noise (∼171 gray values), which correspond to exposure time values ranging between 5 ms and 30 ms. No threshold is applied. The joint probability distribution of photon pairs Γ is calculated by processing the set of images using the formula provided in [32]:

$$\Gamma_{ij} \sim \langle x_i x_j\rangle - \langle x_i\rangle\langle x_j\rangle, \tag{F1}$$

where i and j denote two pixels positions, $\langle x_i x_j\rangle$ is the average value of the product between gray values x_i and x_j of pixels i and j, and $\langle x_i\rangle$ is the average gray value at pixel i. This technique is applicable in this work because the following assumptions are satisfied: (i) Cross-talk between camera pixels is negligible; (ii) the pump laser is operating above threshold to ensure a Poisson distribution of pump photons; (iii) pump laser power is low enough (∼100 mW) to ensure that a >2 photon generation process in the crystal is negligible.

2. Projections of the joint probability distribution

In our experiment, Γ takes the form of a four-dimensional matrix containing $(75 \times 75)^2 \sim 10^8$ elements, where 75×75 corresponds to the size of the illuminated region of the camera sensor. The information content of Γ is analyzed using four types of projections.

(1) The sum-coordinate projection, defined as

$$P_+^\Gamma(\mathbf{k_+}) = \sum_{\mathbf{k}} \Gamma(\mathbf{k}_+ - \mathbf{k}, \mathbf{k}). \tag{F2}$$

It represents the probability of detecting pairs of photons generated in all symmetric directions relative to the mean momentum $\mathbf{k}_+$.

(2) The minus-coordinate projection, defined as

$$P_-^\Gamma(\mathbf{r_-}) = \sum_{\mathbf{r}} \Gamma(\mathbf{r}_- + \mathbf{r}, \mathbf{r}). \tag{F3}$$

It represents the probability for two photons of a pair to be detected in coincidence between pairs of pixels separated by an oriented distance $\mathbf{r}_-$.

(3) The X_+-coordinate projection, defined as

$$P_{X+}^\Gamma(k_{y_1}, k_{y_2}) = \sum_{k_x} \Gamma(k_{y_1}, k_{y_2}|k_x, -k_x) \tag{F4}$$

$$= \sum_{k_x} \frac{\Gamma\big(k_{y_1}, k_{y_2}, k_x, -k_x\big)}{\sum_{k_{x_1},k_{x_2}} \Gamma\big(k_{y_1}, k_{y_2}, k_{x_1}, k_{x_2}\big)}. \tag{F5}$$

It represents the probability of detecting one photon with momentum k_{y_1} (with no constraints on k_{x_1}) given that the other is detected with a momentum k_{y_2} and $k_{x_2} = -k_{x_1}$ (symmetric columns).

(4) The X_--coordinate projection, defined as

$$P_{X-}^\Gamma(y_1, y_2) = \sum_{x} \Gamma(y_1, y_2|x, x+1) \tag{F6}$$

$$= \sum_{x} \frac{\Gamma(y_1, y_2, x, x+1)}{\sum_{x_1,x_2} \Gamma(y_1, y_2, x_1, x_2)}. \tag{F7}$$

It represents the probability of detecting one photon at position y_1 (with no constraints on x_1) given that the other is detected with a momentum y_2 and $x_2 = x_1 + 1$ (adjacent columns).

[1] J. Brendel, N. Gisin, W. Tittel, and H. Zbinden, Phys. Rev. Lett. **82**, 2594 (1999).

[2] P. G. Kwiat, K. Mattle, H. Weinfurter, A. Zeilinger, A. V. Sergienko, and Y. Shih, Phys. Rev. Lett. **75**, 4337 (1995).

[3] J. C. Howell, R. S. Bennink, S. J. Bentley, and R. W. Boyd, Phys. Rev. Lett. **92**, 210403 (2004).

[4] A. Aspect, P. Grangier, and G. Roger, Phys. Rev. Lett. **49**, 91 (1982).

[5] S.-K. Liao, W.-Q. Cai, W.-Y. Liu, L. Zhang, Y. Li, J.-G. Ren, J. Yin, Q. Shen, Y. Cao, Z.-P. Li, F.-Z. Li, X.-W. Chen, L.-H. Sun, J.-J. Jia, J.-C. Wu, X.-J. Jiang, J.-F. Wang, Y.-M. Huang, Q. Wang, Y.-L. Zhou, L. Deng, T. Xi, L. Ma, T. Hu, Q. Zhang, Y.-A. Chen, N.-L. Liu, X.-B. Wang, Z.-C. Zhu, C.-Y. Lu, R. Shu, C.-Z. Peng, J.-Y. Wang, and J.-W. Pan, Nature (London) **549**, 43 (2017).

[6] S. P. Walborn, C. H. Monken, S. Pádua, and P. H. Souto Ribeiro, Phys. Rep. **495**, 87 (2010).

[7] D. S. Tasca, R. M. Gomes, F. Toscano, P. H. Souto Ribeiro, and S. P. Walborn, Phys. Rev. A **83**, 052325 (2011).

[8] S. P. Walborn, D. S. Lemelle, M. P. Almeida, and P. H. Souto Ribeiro, Phys. Rev. Lett. **96**, 090501 (2006).

[9] T. B. Pittman, Y. H. Shih, D. V. Strekalov, and A. V. Sergienko, Phys. Rev. A **52**, R3429 (1995).

[10] G. Brida, M. Genovese, and I. R. Berchera, Nat. Photonics **4**, 227 (2010).

[11] D.-Q. Xu, X.-B. Song, H.-G. Li, D.-J. Zhang, H.-B. Wang, J. Xiong, and K. Wang, Appl. Phys. Lett. **106**, 171104 (2015).

[12] P. B. Dixon, G. A. Howland, J. Schneeloch, and J. C. Howell, Phys. Rev. Lett. **108**, 143603 (2012).

[13] M. Reichert, H. Defienne, X. Sun, and J. W. Fleischer, J. Opt. **19**, 044004 (2017).

[14] C. K. Hong and L. Mandel, Phys. Rev. A **31**, 2409 (1985).

[15] G. Tamošauskas, J. Galinis, A. Dubietis, and A. Piskarskas, Opt. Express **18**, 4310 (2010).

[16] J. Galinis, M. Karpiński, G. Tamosauskas, K. Dobek, and A. Piskarskas, Opt. Express **19**, 10351 (2011).

[17] O. Kwon, K.-K. Park, Y.-S. Ra, Y.-S. Kim, and Y.-H. Kim, Opt. Express **21**, 25492 (2013).

[18] Y.-C. Jeong, K.-H. Hong, and Y.-H. Kim, Opt. Express **24**, 1165 (2016).

[19] M. H. Rubin, Phys. Rev. A **54**, 5349 (1996).

[20] P. H. Souto Ribeiro, Phys. Rev. A **56**, 4111 (1997).

[21] A. Joobeur, B. E. A. Saleh, T. S. Larchuk, and M. C. Teich, Phys. Rev. A **53**, 4360 (1996).

[22] E. J. S. Fonseca, C. H. Monken, S. Pádua, and G. A. Barbosa, Phys. Rev. A **59**, 1608 (1999).

[23] B. E. A. Saleh, M. C. Teich, and A. V. Sergienko, Phys. Rev. Lett. **94**, 223601 (2005).

[24] C. H. Monken, P. H. Souto Ribeiro, and S. Pádua, Phys. Rev. A **57**, 3123 (1998).

[25] G. Kulkarni, P. Kumar, and A. K. Jha, JOSA B **34**, 1637 (2017).

[26] Y. Ismail, S. Joshi, and F. Petruccione, Sci. Rep. **7**, 12091 (2017).

[27] A. K. Jha and R. W. Boyd, Phys. Rev. A **81**, 013828 (2010).

[28] E. Giese, R. Fickler, W. Zhang, L. Chen, and R. W. Boyd, Phys. Scr. **93**, 084001 (2018).

[29] M. V. Fedorov, Phys. Scr. **90**, 074048 (2015).

[30] A. Sanpera, D. Bruß, and M. Lewenstein, Phys. Rev. A **63**, 050301(R) (2001).

[31] B. M. Terhal and P. Horodecki, Phys. Rev. A **61**, 040301(R) (2000).

[32] H. Defienne, M. Reichert, and J. W. Fleischer, Phys. Rev. Lett. **120**, 203604 (2018).

[33] P.-A. Moreau, J. Mougin-Sisini, F. Devaux, and E. Lantz, Phys. Rev. A **86**, 010101(R) (2012).

[34] D. S. Tasca, F. Izdebski, G. S. Buller, J. Leach, M. Agnew, M. J. Padgett, M. P. Edgar, R. E. Warburton, and R. W. Boyd, Nat. Commun. **3**, 984 (2012).

[35] M. Parniak, M. Dabrowski, M. Mazelanik, A. Leszczynski, M. Lipka, and W. Wasilewski, Nat. Commun. **8**, 2140 (2017).

[36] L. Mandel and E. Wolf, Rev. Mod. Phys. **37**, 231 (1965).

[37] M. V. Fedorov, Y. M. Mikhailova, and P. A. Volkov, J. Phys. B **42**, 175503 (2009).

[38] J. Schneeloch and J. C. Howell, J. Opt. **18**, 053501 (2016).

[39] K. W. Chan, J. P. Torres, and J. H. Eberly, Phys. Rev. A **75**, 050101(R) (2007).

[40] M. Reichert, H. Defienne, and J. W. Fleischer, Sci. Rep. **8**, 7925 (2018).

[41] R. Chrapkiewicz, M. Jachura, K. Banaszek, and W. Wasilewski, Nat. Photonics **10**, 576 (2016).

[42] H. Defienne, M. Reichert, and J. W. Fleischer, Phys. Rev. Lett. **121**, 233601 (2018).

[43] Y. Peng, Y. Qiao, T. Xiang, and X. Chen, Opt. Lett. **43**, 3985 (2018).

[44] Y. Qiu and W. She, Appl. Phys. B **108**, 683 (2012).

[45] P. Hong, Appl. Phys. Lett. **113**, 101109 (2018).

[46] C. L. Salter, R. M. Stevenson, I. Farrer, C. A. Nicoll, D. A. Ritchie, and A. J. Shields, Nature (London) **465**, 594 (2010).

[47] W. Zhang, R. Fickler, E. Giese, L. Chen, and R. W. Boyd, arXiv:1812.9532.